

Article

# Design and Preparation of NiFe<sub>2</sub>O<sub>4</sub>@FeOOH Composite Electrocatalyst for Highly Efficient and Stable Oxygen Evolution Reaction

Tian-Tian Li <sup>1,†</sup>, Bu-Yan Shi <sup>1,†</sup>, Li-Wen Jiang <sup>1</sup>, Jin-Fan Zheng <sup>1,\*</sup> and Jian-Jun Wang <sup>1,2,\*</sup> 

<sup>1</sup> State Key Laboratory of Crystal Materials, Department of Neurology, Qilu Hospital, Shandong University, Jinan 250100, China

<sup>2</sup> Shenzhen Research Institute of Shandong University, Shenzhen 518057, China

\* Correspondence: jinfanzheng@sdu.edu.cn (J.-F.Z.); wangjianjun@sdu.edu.cn (J.-J.W.)

† These authors contributed equally to this work.

**Abstract:** Rational design and constructing earth-abundant electrocatalysts for efficient electrocatalytic water splitting is a crucial challenge. Herein, we report a simple and efficient one-step electrochemical synthetic route of the NiFe<sub>2</sub>O<sub>4</sub>@FeOOH composite electrocatalyst for the oxygen evolution reaction. The unique morphology of the NiFe<sub>2</sub>O<sub>4</sub> nanoflowers loaded on FeOOH nanosheets allows more active sites to be exposed and promote charge transfer as well as gas release, and the resulting electrode enables a current density of 10 mA cm<sup>-2</sup> at a low overpotential of 255 mV with outstanding stability at a current density of 100 mA cm<sup>-2</sup> for 300 h.

**Keywords:** oxygen evolution reaction; electrocatalysis; NiFe<sub>2</sub>O<sub>4</sub>; thiourea-assisted synthesis; composite structure



**Citation:** Li, T.-T.; Shi, B.-Y.; Jiang, L.-W.; Zheng, J.-F.; Wang, J.-J. Design and Preparation of NiFe<sub>2</sub>O<sub>4</sub>@FeOOH Composite Electrocatalyst for Highly Efficient and Stable Oxygen Evolution Reaction. *Molecules* **2022**, *27*, 7438. <https://doi.org/10.3390/molecules27217438>

Academic Editors: Pawan Kumar and Devika Laishram

Received: 30 September 2022

Accepted: 27 October 2022

Published: 1 November 2022

**Publisher's Note:** MDPI stays neutral with regard to jurisdictional claims in published maps and institutional affiliations.



**Copyright:** © 2022 by the authors. Licensee MDPI, Basel, Switzerland. This article is an open access article distributed under the terms and conditions of the Creative Commons Attribution (CC BY) license (<https://creativecommons.org/licenses/by/4.0/>).

## 1. Introduction

Hydrogen is considered to be one of the most promising alternates to fossil fuels due to its high energy density and non-pollution during energy conversion [1–3]. The electrolysis of water has attracted a large amount of attention for hydrogen production as well as the efficient storage of renewable energy [4–6]. However, the overall efficiency of water splitting is substantially limited by the sluggish reaction kinetics at the anode, namely, the oxygen evolution reaction (OER) [7–9]. A number of efficient electrocatalysts have been employed to promote the reaction rate of OER, thus improving the overall efficiency of hydrogen production by water splitting [10,11]. Until now, noble metal oxides including IrO<sub>2</sub> and RuO<sub>2</sub> are still considered as the benchmark electrocatalysts for OER due to their excellent electrocatalytic activities [12–15]. In recent years, tremendous effort has been paid to exploring earth-abundant non-noble metal catalysts for OER to avoid the large-scale deployment of precious metals [16–20].

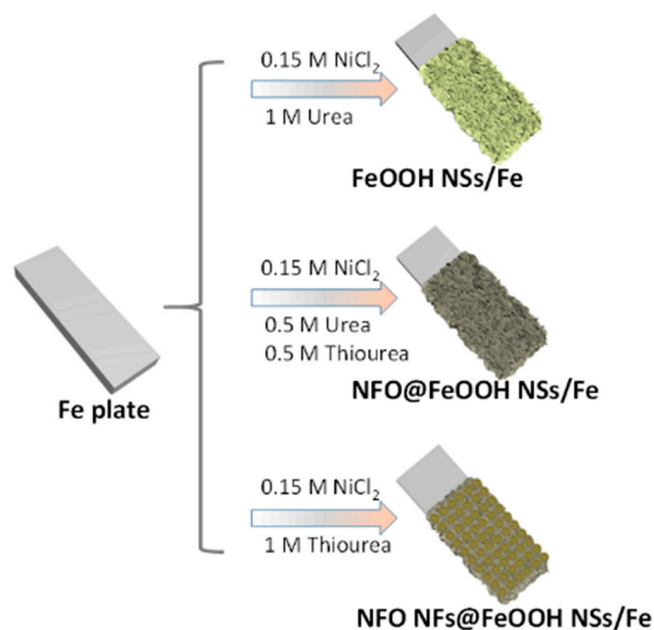
Oxides with spinel structure including Co<sub>3</sub>O<sub>4</sub>, CoFe<sub>2</sub>O<sub>4</sub>, and NiFe<sub>2</sub>O<sub>4</sub> have exhibited great promise as a class of electrocatalysts for OER due to low toxicity, high abundance, flexible ion arrangement, and multivalence structure [21–24]. Among them, NiFe<sub>2</sub>O<sub>4</sub> has been extensively investigated with comparable performance to IrO<sub>2</sub> and RuO<sub>2</sub> [25–27]. For instance, Qiao and co-workers proposed a facile and reliable strategy to synthesize S-NiFe<sub>2</sub>O<sub>4</sub>/NF with thiourea-assisted electrodeposition and the resulting electrode displayed intriguing catalytic properties. By constructing heterojunction with other components, enhanced electrocatalytic activity can be achieved due to the renewed or upgraded active sites [28]. Gao et al. developed a facile solvothermal approach to decorate the NiFe LDH nanosheet with NiFe<sub>2</sub>O<sub>4</sub> nanoparticles to form a heterostructure array on Ni foam, leading to significantly enhanced mass and charge transfer efficiency as well as the active surface [29]. Similar results were also observed from the composite electrocatalyst

of FeNi/NiFe<sub>2</sub>O<sub>4</sub>/NC polyhedron-assembled microboxes derived from the carbonization of bimetal MOF [30]. Recently, our group reported the highly efficient and stable NiFe<sub>2</sub>O<sub>4</sub>-xSe<sub>x</sub>/NiOOH electrocatalyst on stainless steel for OER and the precise selenization of NiFe<sub>2</sub>O<sub>4</sub> significantly boosted the OER performance. Apart from enhancing the intrinsic activity, enlarging the electrocatalytically active area and magnifying the number of active sites are of comparable importance in improving the performance of target electrodes [31–34]. Additionally, the efficiency of charge and mass transfer critically dictates the electrocatalytic activity for OER [35]. All of the aforementioned aspects concurrently contribute to the improved OER performance and thus simultaneously addressing these issues is highly desirable, but challenging.

Herein, we report on an intriguing composite electrocatalyst with spinel NiFe<sub>2</sub>O<sub>4</sub> nanoflowers loaded on FeOOH nanosheets for OER and the resulting electrode exhibited excellent OER activity and good stability at a relatively high current density. The designed composite structure endowed the electrode with the enhanced specific surface area, consequently allowing for more active sites and efficient charge transfer as well as gas release. Electrochemical experiments demonstrated that the optimized NFO NFs@FeOOH NSs/Fe electrocatalyst showed enhanced electrocatalytic activity and enabled a current density of 10 mA cm<sup>-2</sup> at an overpotential of 255 mV and outstanding stability at 100 mA cm<sup>-2</sup> for 300 h. The study on mechanism revealed that thiourea has an important role during the electrochemical deposition process and significantly affects the composition and crystal structure of the composite.

## 2. Results and Discussion

The synthetic procedure of samples through a facile one-step electrodeposition method is displayed in Scheme 1. It was found that the electrolyte used is critical to the structure and morphology of the resulting samples. Typically, clean Fe plates are put into three kinds of electrolyte containing urea, thiourea, and their mixture with a ratio of 1:1 to obtain FeOOH nanosheets/Fe, NiFe<sub>2</sub>O<sub>4</sub>@FeOOH nanosheets/Fe, and NiFe<sub>2</sub>O<sub>4</sub> nanoflowers@FeOOH nanosheets/Fe, which were denoted as FeOOH NSs/Fe, NFO@FeOOH NSs/Fe, and NFO NFs@FeOOH NSs/Fe, respectively. After drying in the air at room temperature for 12 h, the color of the samples turned into light yellow, brown yellow, and black, respectively, as shown in Figure S1.



**Scheme 1.** The schematic diagram of the synthesis of FeOOH NSs/Fe, NFO@FeOOH NSs/Fe, and NFO NFs@FeOOH NSs/Fe on the Fe plate via a one-step method.

The crystal structure of the samples was first studied by XRD and Raman. In Figure 1a, stronger peaks at  $44.67^\circ$ ,  $65.02^\circ$  and  $82.33^\circ$  were observed for all of the samples due to the (110), (200), and (211) facets of the substrate Fe plates (JCPDS No. 06-0696), respectively. In general, two sets of peaks can be observed (Figure 1a). One set of peaks at  $18.39^\circ$ ,  $30.29^\circ$ ,  $35.69^\circ$ ,  $37.31^\circ$ ,  $43.36^\circ$ ,  $47.50^\circ$ ,  $53.80^\circ$ ,  $57.36^\circ$ ,  $62.91^\circ$ ,  $66.23^\circ$ ,  $71.48^\circ$ ,  $74.63^\circ$ ,  $75.56^\circ$ , and  $79.58^\circ$  can be ascribed to the spinel  $\text{NiFe}_2\text{O}_4$  structure (JCPDS No. 10-0325) and the other set of peaks at  $14.11^\circ$ ,  $27.05^\circ$ ,  $36.29^\circ$ ,  $36.90^\circ$ , and  $46.77^\circ$  can be assigned to the  $\text{FeOOH}$  structure (JCPDS No. 44-1415). When pure urea was used, only the  $\text{FeOOH}$  signal was observed, suggesting that urea is profitable for the formation of  $\text{FeOOH}$ . In contrast,  $\text{NiFe}_2\text{O}_4$  and  $\text{FeOOH}$  were formed when thiourea was introduced into the electrolyte. The stronger intensity of  $\text{NiFe}_2\text{O}_4$  peaks than the  $\text{FeOOH}$  peaks indicates that thiourea is in favor of the formation of  $\text{NiFe}_2\text{O}_4$ . Additionally, the Raman spectra further consolidated the important role of thiourea on the structure and composition of the electrocatalysts. As shown in Figure 1b, the Raman peaks at  $\sim 213.6$ ,  $275.1$ ,  $379.9$ , and  $582.7 \text{ cm}^{-1}$  of the sample obtained with urea are consistent with the standard  $\text{FeOOH}$  peaks [36]. In contrast, the five Raman peaks at  $\sim 205.0$ ,  $330.0$ ,  $485.2$ ,  $560.5$ , and  $695.1 \text{ cm}^{-1}$  of the sample synthesized with thiourea (Figure 1c) can well be assigned to spinel  $\text{NiFe}_2\text{O}_4$ , in good agreement with the observations from XRD. No characteristic peaks of  $\text{NiOOH}$  and  $\text{Ni}(\text{OH})_2$  were observed, which may be explained by the smaller solubility constant of  $\text{Fe}(\text{OH})_3$  than that of  $\text{Ni}(\text{OH})_2$ , limiting the formation of  $\text{Ni}(\text{OH})_2$  and  $\text{NiOOH}$ . Therefore, the component of the resulting composite can be readily controlled by regulating the electrolyte [25,37,38].

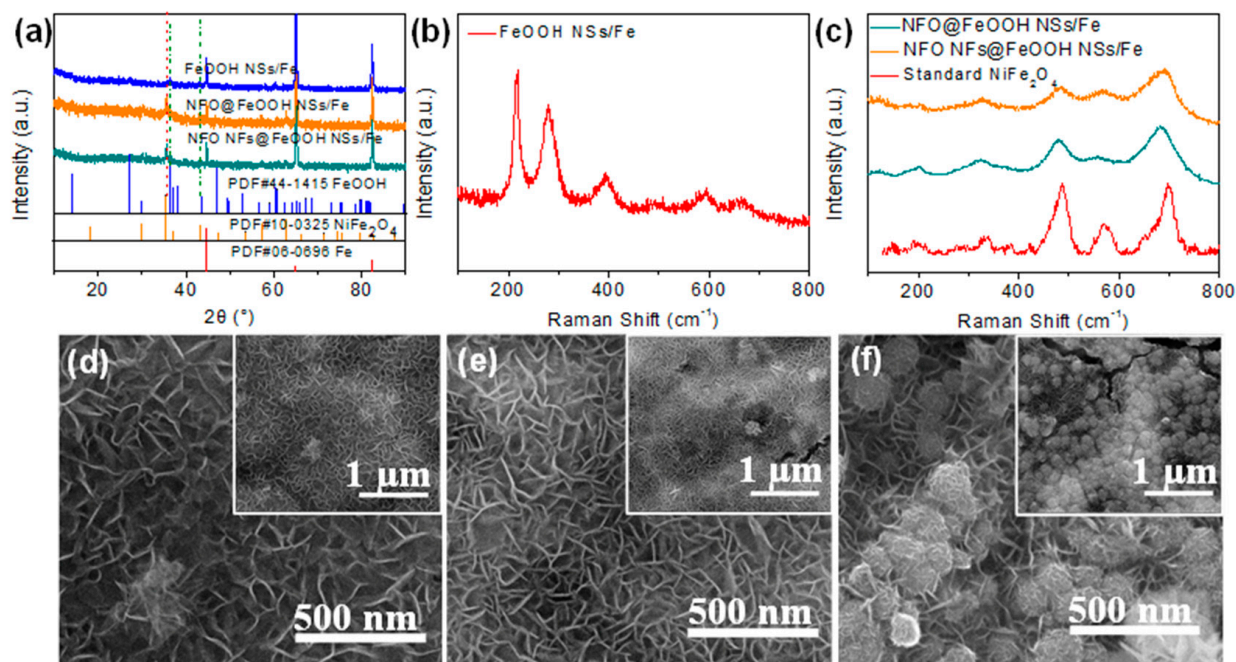


**Figure 1.** Sample characterizations. (a) XRD patterns of  $\text{FeOOH NSs/Fe}$ ,  $\text{NFO@FeOOH NSs/Fe}$ , and  $\text{NFO NFs@FeOOH NSs/Fe}$ ; (b) Raman spectrum of  $\text{FeOOH NSs/Fe}$ ; (c) Raman spectrum of  $\text{NFO@FeOOH NSs/Fe}$ ,  $\text{NFO NFs@FeOOH NSs/Fe}$ , and standard spinel structures  $\text{NiFe}_2\text{O}_4$ ; the SEM images of (d)  $\text{FeOOH NSs/Fe}$ ; (e)  $\text{NFO@FeOOH NSs/Fe}$ , and (f)  $\text{NFO NFs@FeOOH NSs/Fe}$ .

The morphology of the samples was studied using scanning electron microscopy (SEM) (Figure 1d–f). Clearly,  $\text{FeOOH}$  nanosheets were uniformly coated on Fe plates when the sample was prepared using urea (Figure 1d). Nanoflowers loaded on  $\text{FeOOH}$  nanosheets were observed due to the formation of  $\text{NiFe}_2\text{O}_4$  assisted by thiourea (Figure 1e,f). In general, the nanoflowers are considered to be formed by the combinatorial attachment of nanoparticles or nanoplates on the existing crystal seeds due to the electrostatic interaction. Therefore, we believe that the plate-like nuclei are preferentially formed, and these plate-like nuclei

are self-assembled to form flower-like crystal seeds, which are further grown to form nanoflowers. This result further proves that thiourea can regulate the morphology of the resulting samples. On the other hand, as previously reported, the deposition potential of Ni can be negatively shifted due to the depolarization effect. Clearly, the introduction of thiourea showed a critical effect on the electrodeposition process of Ni, enabling the control of Ni content in the products. Compared with the simple nanosheets, the composite structure composed of three-dimensional nanoflowers and two-dimensional nanosheets provided a larger surface area, endowing the electrode with more active sites and channels for rapid charge and mass transfer and bubble release, thus improving the catalytic performance [39,40].

The morphology and structure of the samples were further studied using transmission electron microscopy (TEM). As shown in Figure 2a,b, a composite structure of nanoflowers attached to nanosheets was observed and the nanoflowers were constituted of nanoparticles. The observed d-spacings of 0.482 and 0.251 nm can be ascribed to (111) and (311) planes of  $\text{NiFe}_2\text{O}_4$  (JCPDS No. 10-0325), respectively, proving that the composition of nanoparticles is spinel  $\text{NiFe}_2\text{O}_4$  (Figure 2c,d). Additionally, the selected area electron diffraction (SAED) pattern recorded from the region in Figure 2f indicated that the composite contained  $\text{NiFe}_2\text{O}_4$  and  $\text{FeOOH}$ . The rings can be assigned to (222), (622), (551) of  $\text{NiFe}_2\text{O}_4$  and (101), (220), (121) of  $\text{FeOOH}$ , respectively. The elemental mapping in Figure 2g indicated that the elements of Fe, Ni, O, and S were uniformly distributed within the NFO NFs@ $\text{FeOOH}$  NSs/Fe composite electrocatalysts. Apparently, the contents of Ni and S were significantly less than Fe and O, consistent with sulfur-doped  $\text{NiFe}_2\text{O}_4$  and the  $\text{FeOOH}$  composite electrocatalyst as prepared. The results of TEM and SAED confirmed the crystal structure and components of the NFO NFs@ $\text{FeOOH}$  NSs/Fe electrocatalyst, consistent with the results of XRD and Raman. The ratio of  $\text{FeOOH}$  and  $\text{NiFe}_2\text{O}_4$  in NFO NFs@ $\text{FeOOH}$  NSs/Fe was determined by TGA (Figure S2). Generally, the weight loss stage from 200 °C to 350 °C is mainly attributed to the dehydration of  $\text{FeOOH}$  to  $\text{Fe}_2\text{O}_3$  [41,42]. Therefore, the contents of  $\text{FeOOH}$  and  $\text{NiFe}_2\text{O}_4$  in the composite were calculated to be 4.04% and 95.96%, respectively.

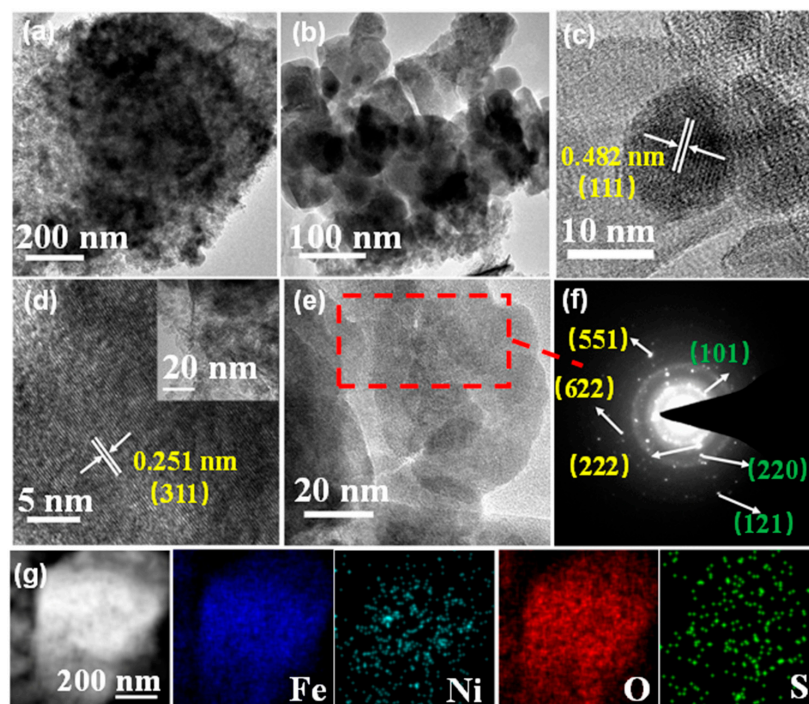


**Figure 2.** (a,b) TEM images of NFO NFs@ $\text{FeOOH}$  NSs/Fe; (c,d) HRTEM images of NFO NFs@ $\text{FeOOH}$  NSs/Fe. (e,f) The selected area electron diffraction pattern of NFO NFs@ $\text{FeOOH}$  NSs/Fe. (g) STEM images of NFO NFs@ $\text{FeOOH}$  NSs/Fe, and elemental mappings of Fe, O, Ni, and S.

The surface composition and chemical states of NFO NFs@FeOOH NSs/Fe were further investigated by XPS. The survey spectrum of NFO NFs@FeOOH NSs/Fe (Figure S3) suggests that the elements of Fe, Ni, O, and S are present, consistent with the elemental mapping analysis. In Figure 3a, the peaks at 710.9 eV ( $\text{Fe}^{3+}$  2p<sub>3/2</sub>), 712.2 eV ( $\text{Fe}^{2+}$  2p<sub>3/2</sub>), 723.7 eV ( $\text{Fe}^{3+}$  2p<sub>1/2</sub>), and 725.8 eV ( $\text{Fe}^{2+}$  2p<sub>1/2</sub>), along with the two satellite peaks at 718.9 eV and 732.0 eV in the Fe 2p regions, indicates the presence of  $\text{Fe}^{3+}$  and  $\text{Fe}^{2+}$ , consistent with previous reports. With regard to the Ni 2p spectrum, the peaks observed at 855.7 and 873.1 eV were attributed to the spin–orbit doublets of Ni 2p<sub>3/2</sub> and Ni 2p<sub>1/2</sub>, respectively (Figure 3b), along with two satellite peaks at 861.4 and 879.2 eV, characteristic of  $\text{Ni}^{2+}$  [27]. For the O1s spectrum displayed in Figure 3c, the two peaks at 529.5 and 530.9 eV were attributed to the M–O and M–O–H bonds, respectively, further supporting the presence of  $\text{NiFe}_2\text{O}_4$  and FeOOH [43]. Notably, a peak at 531.5 eV was observed, which is likely due to the C=O bond of urea, which is caused by the decomposition of thiourea during electrodeposition [28]. The two small peaks at 162.5 and 163.7 eV corresponding to S 2p<sub>3/2</sub> and S 2p<sub>1/2</sub> of M–S bond, respectively, confirms the presence of S with a broad peak at about 168.0 eV due to surface oxidation (Figure 3d). Similar results were observed from the samples of FeOOH NSs/Fe and NFO@FeOOH NSs/Fe (Figures S4 and S5), further confirming the composite structure.

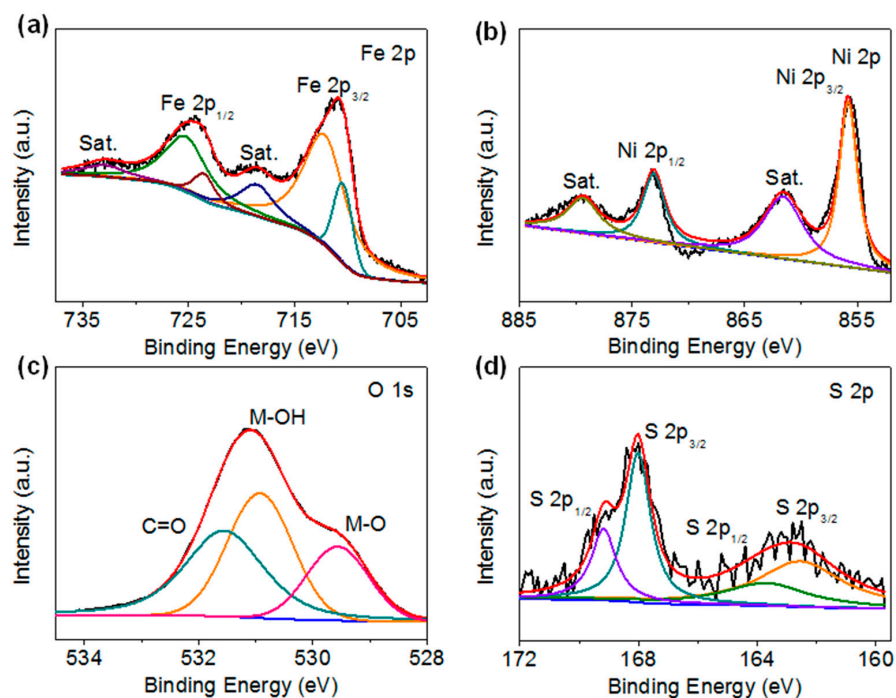


**Figure 3.** The high-resolution XPS spectra of (a) Fe 2p; (b) Ni 2p; (c) O 1s; and (d) S 2p for NFO NFs@FeOOH NSs/Fe.

To study the electrocatalytic performance of the as-prepared electrodes, a series of electrochemical characterization were carried out in 1 M KOH alkaline electrolyte. Figure 4a displays the linear sweep voltammetry (LSV) polarization curves recorded at  $5 \text{ mV s}^{-1}$ . Clearly, the NFO NFs@FeOOH NSs/Fe composite electrocatalysts showed a significant enhanced OER performance compared with the control samples. Notably, the reduction peak between 1.3 and 1.4V(vs.RHE) is likely due to the transformation from  $\text{Ni}^{3+}$  to  $\text{Ni}^{2+}$  [44,45]. To deliver a current density of  $10 \text{ mA cm}^{-2}$ , an overpotential of 255 mV is required for the NFO NFs@FeOOH NSs/Fe electrode, lower than FeOOH NSs/Fe (290 mV) and NFO@FeOOH NSs/Fe (267 mV). The improved OER activity of NFO NFs@FeOOH NSs/Fe was further confirmed by the Tafel plot obtained from the LSV curves according to the Tafel equation. The Tafel slope of NFO NFs@FeOOH NSs/Fe catalysts was  $33.96 \text{ mV dec}^{-1}$ , which is lower than that of the FeOOH NSs/Fe ( $41.34 \text{ mV dec}^{-1}$ ) and NFO@FeOOH

NSs/Fe ( $38.66 \text{ mV dec}^{-1}$ ), further indicating an improved reaction kinetics for OER [46]. The superior OER performance of NFO NFs@FeOOH NSs/Fe was even better than those of many reported promising non-precious metal oxide catalysts (Figure S10 and Table S2). The Faraday efficiency was calculated by measuring the amount of  $\text{O}_2$  generated using gas chromatography. In Figure 4c, a Faraday efficiency of about 95% was achieved for NFO NFs@FeOOH NSs/Fe (the calculation formula is shown in the Supplementary Materials S1), illustrating that the current truly originated from the OER process [47]. In addition, the long-term stability is critical for the practical application of OER electrocatalysts. The chronoamperometry tests indicates that NFO NFs@FeOOH NSs/Fe exhibited good stability with negligible loss for 300 h at a large current density of  $100 \text{ mA cm}^{-2}$ . After the stability test, the catalyst displayed a comparable LSV curve to the one initially recorded (the inset of Figure 4d), implying that the excellent activity remains at a high current density in alkaline solution. The morphology of nanoflowers loaded on FeOOH nanosheets were well maintained during the stability tests at 80 h and 200 h (Figures S6 and S7), demonstrating the good structural stability of NFO NFs@FeOOH NSs/Fe.

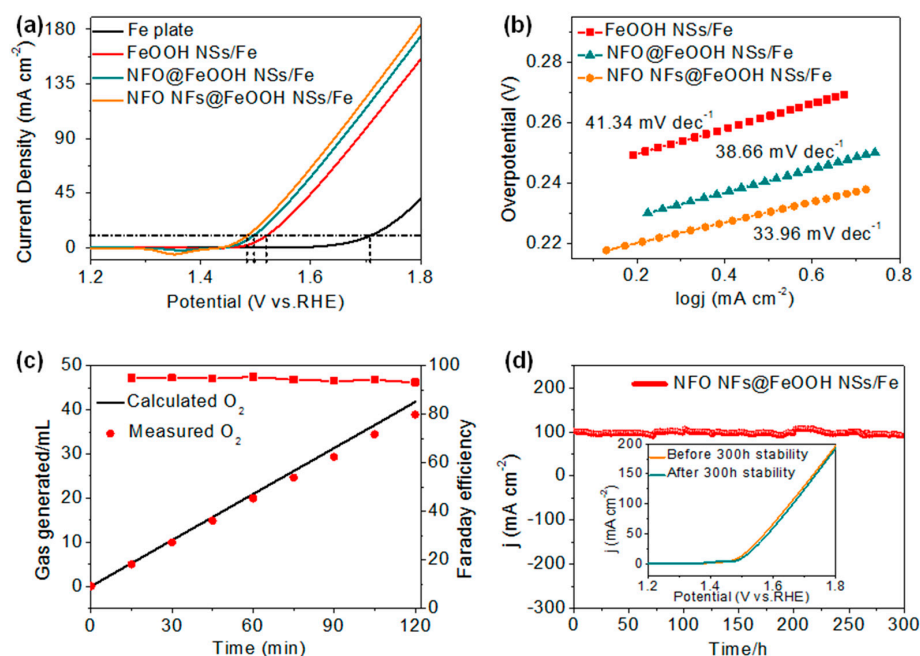


**Figure 4.** (a) Polarization curves of the Fe plate, FeOOH NSs/Fe, NFO@FeOOH NSs/Fe, and NFO NFs@FeOOH NSs/Fe in a 1 M KOH alkaline solution with a scan rate of  $5 \text{ mV s}^{-1}$  (without IR correction). (b) The corresponding Tafel plots; (c) the Faraday efficiency of NFO NFs@FeOOH NSs/Fe. (d) Stability of NFO NFs@FeOOH NSs/Fe at  $100 \text{ mA cm}^{-2}$ .

Electrochemical impedance spectroscopy (EIS) was further performed on electrocatalysts to further study the OER kinetics and charge transfer process. The obtained Nyquist plots were fitted using an equivalent circuit (Figure S8) including a solution resistance ( $R_s$ ) connected in series with two parallel combinations of resistors ( $R_f$ ,  $R_{ct}$ ) and constant-phase elements (CPE1, CPE2), where  $R_f$  signifies the charge transfer at the substrate/catalyst junction and  $R_{ct}$  stands for the charge transfer process at the interface of the catalyst/electrolyte [48,49]. The fitting values of  $R_s$ ,  $R_f$ , and  $R_{ct}$  are shown in Table S1. As shown in Figure 5a, all three samples showed a similar low value ( $\sim 1.0 \text{ ohm}$ ) of  $R_f$ , suggesting that self-supported electrocatalysts synthesized by the one-step deposition methods ensured tight contact of the catalyst and substrate, and promoted the charge transfer process at the interface of the catalyst/electrolyte. In contrast, the  $R_{ct}$  of NFO NFs@FeOOH NSs/Fe ( $1.95 \text{ ohm}$ ) was significantly lower than FeOOH NSs/Fe ( $7.05 \text{ ohm}$ ) and NFO@FeOOH NSs/Fe ( $2.25 \text{ ohm}$ ), suggesting a faster charge transfer rate at the catalyst/electrolyte interface. The results of EIS demonstrated that the unique composite

structure of the NFO NFs@FeOOH NSs/Fe electrocatalyst is conducive to reducing the charge transfer resistance at the interface, thus accelerating the charge transfer rate and improving the activity of OER. To better evaluate the intrinsic electrocatalytic activity of NFO NFs@FeOOH NSs/Fe, their electrochemical double-layer capacitance ( $C_{dl}$ ) was measured to evaluate the electrochemical active surface area (ECSA) (Figure S9) [50]. In Figure 5b, NFO NFs@FeOOH NSs/Fe exhibited a  $C_{dl}$  of  $78.5 \text{ mF cm}^{-2}$ , which was much higher than that of NFS@FeOOH NSs/Fe ( $45.0 \text{ mF cm}^{-2}$ ), and twice that of FeOOH NSs/Fe ( $36.8 \text{ mF cm}^{-2}$ ) (the calculation formula is shown in the Supplementary Materials S2). The result of ECSA indicates that the composite electrocatalysts possesses a bigger electrochemical active surface area and consequently provides more active sites. We measured the linear sweep voltammetry (LSV) curves under automatic iR correction, as shown in Figure 5c, and NFO NFs@FeOOH NSs/Fe still displayed better OER performance than FeOOH NSs/Fe and NFO@FeOOH NSs/Fe after iR correction. Then, the iR-corrected LSV curves were normalized by ECSA to further evaluate the intrinsic activity of the samples, as displayed in Figure 5d. Notably, the LSV curve of NFO NFs@FeOOH NSs/Fe was still significantly improved compared with FeOOH NSs/Fe, but very close to NFO@FeOOH NSs/Fe after the normalization, implying that the spinel  $\text{NiFe}_2\text{O}_4$  enhances the intrinsic OER activity while the unique nanoflower morphology merely exposes more ECSA without obvious effects on the intrinsic activity [51]. This further confirms that the amplified surface area of NFO NFs@FeOOH NSs/Fe composite electrocatalysts has an essential role in the improvement of OER performance, which provides more active sites, shortens the transport pathway, and accelerates OER kinetics [19,52,53]. From the EIS and ECSA results, it is clear that the unique composite structure of the NFO NFs@FeOOH NSs/Fe electrocatalyst is conducive to reducing the charge transfer resistance, thus accelerating the charge transfer rate. Moreover, compared with FeOOH NSs/Fe and NFO@FeOOH NSs/Fe nanosheet structures, NFO NFs@FeOOH NSs/Fe with a unique composite structure has a larger specific surface area, increasing the number of active sites and the contact area between the electrode and the electrolyte, which is beneficial to improving the OER performance. Additionally, the doped S can further improve the intrinsic conductivity of NFO NFs@FeOOH NSs/Fe [28]. The synergistic effect between Ni and Fe also has an essential role in improving the performance of NFO NFs@FeOOH NSs/Fe, which can regulate the electronic structure and optimize the adsorption energy of the intermediate during the OER process [54–56].

To understand the OER activation energy ( $E_a$ ) of the prepared samples, LSV curves at varying temperatures were measured to evaluate the kinetic barriers of the corresponding OER process. In general, the reaction rate is gradually accelerated when the temperature increases (Figure 6a–c).  $E_a$  of different catalysts was calculated according to the Arrhenius relationship [57]. As shown in Figure 6d,  $E_a$  of NFO NFs@FeOOH NSs/Fe was  $21.63 \text{ kJ mol}^{-1}$ , much lower than FeOOH NSs/Fe ( $32.54 \text{ kJ mol}^{-1}$ ) and comparable to NFO@FeOOH NSs/Fe ( $21.72 \text{ kJ mol}^{-1}$ ), further confirming the superiority of the unique composite structure.

According to the above analyses, the enhanced performance of NFO NFs@FeOOH NSs/Fe catalysts can be ascribed to the following aspects. First, the Tafel slope of NFO NFs@FeOOH NSs/Fe was lower than that of NFO@FeOOH NSs/Fe and FeOOH NSs/Fe, indicating that NFO NFs@FeOOH NSs/Fe possesses faster OER reaction kinetics. Second, the NFO NFs@FeOOH NSs/Fe unique composite catalysts with nanoflowers loaded on nanosheets allowed for a larger active area with more active sites, which is also an important factor for the excellent OER performance of NFO NFs@FeOOH NSs/Fe. In addition, the NFO NFs@FeOOH NSs/Fe composite electrocatalyst possessed lower charge transfer resistance, which accelerates the charge transfer and improves the electrical conductivity. Finally, in light of the Arrhenius relationship, the lower activation energy barrier value of NFO NFs@FeOOH NSs/Fe confirmed the higher intrinsic catalytic activity. Based on the experimental results and literature reports, the unique composite structure of NFO NFs@FeOOH NSs/Fe can be attributed to the following two reasons. According to the experimental results, it can be seen that urea and thiourea have a great influence on the

morphology of the catalysts. A large number of studies have reported that thiourea can be decomposed into sulfur ions and urea during the electrodeposition process, which plays a regulatory role in the growth of nanocrystals. Therefore, the effect of thiourea is one of the important reasons for the formation of the unique composite structure of nanoflowers loaded on nanosheets. Additionally, the synergistic effect of Fe and Ni plays an important role in the regulation of surface morphology, which can expose more active sites, accelerate charge transfer, and improve electrical conductivity.

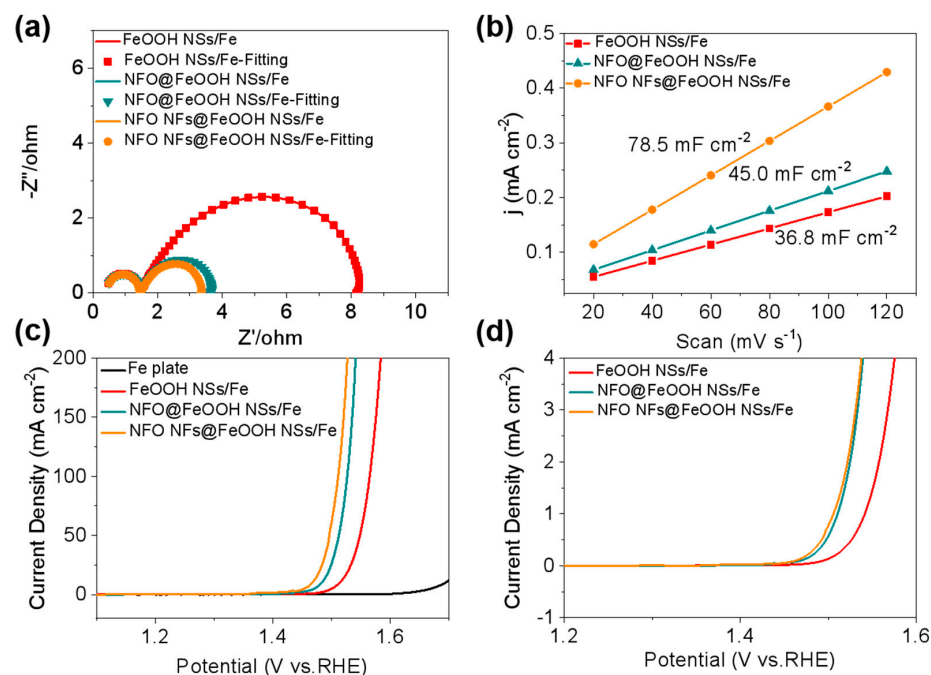


**Figure 5.** (a) Nyquist plots; (b)  $C_{dl}$  linear fitting and calculations of ECSA. (c) Polarization curves with 100% iR compensate, and the corresponding (d) ECSA normalized polarization curves.

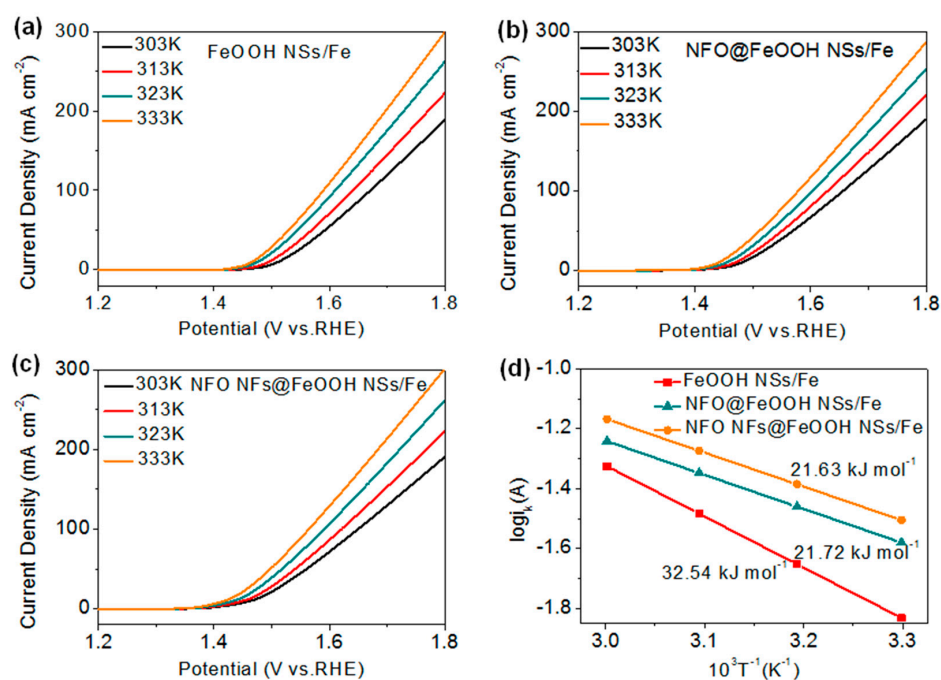


**Figure 6.** Polarization curves of (a) FeOOH NSs/Fe; (b) NFO@FeOOH NSs/Fe; and (c) NFO NFs@FeOOH NSs/Fe recorded at  $5 \text{ mV s}^{-1}$  at 303 K, 313 K, 323 K, and 333 K, respectively. (d) Arrhenius plots.

### 3. Materials and Methods

#### 3.1. Chemicals and Materials

Nickel chloride ( $\text{NiCl}_2 \cdot 6\text{H}_2\text{O}$ ) was obtained from Macklin (Shanghai, China) and urea ( $\text{CH}_4\text{N}_2\text{O}$ ) and potassium hydroxide (KOH) were obtained from the National Reagent Company. The commercial Fe plate (Fe content: 99.9%, thickness: 0.3 mm) was purchased from Guantai Metal Materials Co. Ltd. (Shenzhen, China). Deionized water (18.2 M $\Omega$  cm) was utilized throughout all of the experiments. All of the chemicals were analytical grade (AR) and used without additional purification.

#### 3.2. Synthesis of FeOOH NSs/Fe, NFO@FeOOH NSs/Fe, and NFO NFs@FeOOH NSs/Fe Catalysts

Fe plates (3 cm  $\times$  1 cm) were used as the substrate, which were cleaned using acetone and ethyl alcohol successively for 15 min, and finally vacuum drying at 50 °C.  $\text{NiFe}_2\text{O}_4$  nanoflowers@FeOOH nanosheets/Fe was prepared via thiourea-assisted electrodeposition [28,58]. In a typical procedure, 0.05 M  $\text{NiCl}_2$  and 1 M thiourea were mixed in 100 mL of deionized water to prepare the electrolyte solution. The electrodeposition was performed in a three-electrode cell with a CHI660E electrochemical workstation. The cleaned Fe plate, carbon rod, and Ag/AgCl electrode were utilized as the working electrode, counter electrode, and reference electrode, respectively. The deposition started at  $-0.9$  V for 6 s and then shifted to 0.1 V for 24 s, and repeated 20 times. After electrodeposition, the sample was cleaned with deionized water and ethyl alcohol several times and then naturally dried in air. For the comparative study, the FeOOH nanosheets/Fe samples were fabricated with the electrolyte containing 1 M urea, and  $\text{NiFe}_2\text{O}_4$ @FeOOH nanosheets/Fe samples were fabricated with the electrolyte containing 0.5 M urea and 0.5 M thiourea. Other steps were similar to the procedure described above. The addition of  $\text{Ni}^{2+}$  can regulate the electrodeposition process to avoid the formation of  $\text{Fe}_3\text{O}_4$ .

#### 3.3. Material Characterization

The X-ray diffraction (XRD) patterns of samples were recorded on a SmartLab SE Advanced X-ray diffractometer (Smartlab3KW) with Cu K $\alpha$  radiation ( $\lambda = 1.5418$  Å). The X-ray photoelectron spectroscopy (XPS) spectrum was collected by ESCALAB 250. All of the XPS spectra were calibrated using C 1s of 284.6 eV. The Raman spectra (HORIBA LabRAM HR Evolution) were obtained using an excitation laser at 532 nm with a laser power of 2 mW. The surface morphologies of the samples were studied with a scanning electron microscope (SEM, Zeiss EVO18). Transmission electron microscopy (TEM), high resolution TEM (HRTEM, Talos F200x), and selected area electron diffraction (SAED) were also used to characterize the microstructures of the samples.

#### 3.4. Electrochemical Characterizations

The electrocatalytic properties of the NFO NFs@FeOOH NSs/Fe electrocatalysts were studied in a three-electrode cell with a 1 M KOH solution as the electrolyte. A platinum plate and Ag/AgCl (3.3 M KCl) were utilized as the counter electrode and reference electrode, respectively. The as-prepared electrodes were utilized as the working electrode. The potentials used in this study were converted to ERHE from  $E_{\text{Ag}/\text{AgCl}}$  according to the formula  $E_{\text{RHE}} = E_{\text{Ag}/\text{AgCl}} + 0.197 + 0.05916 \times \text{pH}$ . The polarization curves were tested at 5 mV/s. The iR compensation with a value of 100%  $\times$  Ru was conducted by the automatic current interrupt method on the working station (CHI660E). Chronopotentiometry measurements were performed at 1.66 V vs. RHE in 1.0 M KOH to evaluate the stability. The Faradaic efficiency was calculated by  $\text{O}_2$  generation at 1.23 V vs. RHE in 1 M KOH, which was measured by gas chromatography. For comparison, the electrocatalytic activities of the Fe plate, FeOOH NSs/Fe, and NFO@FeOOH NSs/Fe samples were also measured under similar conditions. All of the experiments were carried out at ambient temperature ( $\sim 300$  K) and the test area for all samples was 1 cm  $\times$  1 cm.

#### 4. Conclusions

A facile one-step electrodeposition method was developed to synthesize  $\text{NiFe}_2\text{O}_4/\text{FeOOH}$  composite electrocatalysts for efficient OER. The morphology and component of the resulting electrocatalysts can be readily controlled by changing the ratio of thiourea and urea in the electrolyte. The as-prepared electrocatalysts were studied and confirmed with XRD, SEM, TEM, and XPS. Electrochemical measurements indicate that the designed NFO NFs@FeOOH NSs/Fe composite electrocatalysts delivered a greatly improved catalytic performance for OER with a low overpotential of 255 mV to achieve a current density of  $10 \text{ mA cm}^{-2}$ . Importantly, the resulting electrode exhibited a high stability for OER, allowing for at least 300 h at  $100 \text{ mA cm}^{-2}$  with negligible decay. The improved performance can be ascribed to the unique composite structure that endowed the electrode with the enhanced conductivity and specific surface area, and was consequently beneficial to electron transmission and the exposure of more active sites. This synthetic approach allows for the facile fabrication of composite OER electrocatalysts with a large surface area and good conductivity and may be extended to other potential electrodes for commercial applications.

**Supplementary Materials:** The following supporting information can be downloaded at: <https://www.mdpi.com/article/10.3390/molecules27217438/s1>, Figure S1: The photographs of the FeOOH NSs/Fe, NFO@FeOOH NSs/Fe, and NFO NFs@FeOOH NSs/Fe samples after electrodeposition and dried in air; Figure S2: Thermogravimetric analysis curve of NFO NFs@FeOOH NSs/Fe; Figure S3: The XPS survey spectrum of NFO NFs@FeOOH NSs/Fe; Figure S4: (a) XPS survey spectrum and high-resolution XPS spectra of (b) Fe 2p, (c) Ni 2p, and (d) O 1s for FeOOH NSs/Fe; Figure S5: (a) XPS survey spectrum and high-resolution XPS spectra of (b) Fe 2p, (c) Ni 2p, and (d) O 1s for NFO@FeOOH NSs/Fe; Figure S6: SEM image of NFO NFs@FeOOH NSs/Fe after 80 h of stability measurement; Figure S7: SEM image of NFO NFs@FeOOH NSs/Fe after 200 h of stability measurement; Figure S8: The equivalent circuit used for fitting of Nyquist plots; Figure S9: CV curves at different scan rates. (a) FeOOH NSs/Fe, (b) NFO@FeOOH NSs/Fe, and (c) NFO NFs@FeOOH NSs/Fe; Figure S10: Comparison of the OER performance of NFO NFs@FeOOH NSs/Fe with the recently reported non-precious metal oxide catalysts in 1.0 M KOH electrolyte; Table S1: The obtained values of  $R_s$ ,  $R_f$ , and  $R_{ct}$  by fitting; Table S2: Comparison of the OER performance in the 1.0 M KOH electrolyte. [27,28,41,42,48,59–65] are cited in the supplementary materials.

**Author Contributions:** T.-T.L. and B.-Y.S. contributed equally to the preparation of the original draft; L.-W.J., Visualization; J.-F.Z. and J.-J.W. proposed, supervised, and edited this work. All authors have read and agreed to the published version of the manuscript.

**Funding:** This work was funded by the National Natural Science Foundation of China (Grant No. 22279075); Shandong Provincial Natural Science Foundation (Grant No. ZR2019MB048, ZR2020YQ09); QiLu Young Scientist Program of Shandong University, and Shenzhen Fundamental Research Program (No. JCYJ20190807093411445).

**Institutional Review Board Statement:** Not applicable.

**Informed Consent Statement:** Not applicable.

**Data Availability Statement:** Not applicable.

**Conflicts of Interest:** The authors declare no conflict of interest.

**Sample Availability:** Sample of the compounds are not available.

#### References

1. Li, G.; Dang, C.; Hou, Y.; Dang, F.; Fan, Y.; Guo, Z. Experimental and Theoretical Characteristic of Single Atom Co-N-C Catalyst For Li-O<sub>2</sub> Batteries. *Eng. Sci.* **2020**, *10*, 85–94. [[CrossRef](#)]
2. Padvi, M.N.; Moholkar, A.V.; Prasad, S.R.; Prasad, N.R. A Critical Review on Design and Development of Gas Sensing Materials. *Eng. Sci.* **2021**, *15*, 20–37. [[CrossRef](#)]
3. Zhao, J.; Wei, D.; Zhang, C.; Shao, Q.; Murugadoss, V.; Guo, Z.; Jiang, Q.; Yang, X. An Overview of Oxygen Reduction Electrocatalysts for Rechargeable Zinc-Air Batteries Enabled by Carbon and Carbon Composites. *Eng. Sci.* **2021**, *15*, 1–19. [[CrossRef](#)]

4. Jiang, Y.; Huang, J.; Mao, B.; An, T.; Wang, J.; Cao, M. Inside solid-liquid interfaces: Understanding the influence of the electrical double layer on alkaline hydrogen evolution reaction. *Appl. Catal. B* **2021**, *293*, 120220. [[CrossRef](#)]
5. Zhu, J.; Hu, L.; Zhao, P.; Lee, L.Y.S.; Wong, K.Y. Recent Advances in Electrocatalytic Hydrogen Evolution Using Nanoparticles. *Chem. Rev.* **2020**, *120*, 851–918. [[CrossRef](#)] [[PubMed](#)]
6. Singh, N.; Jana, S.; Singh, G.P.; Dey, R.K. Graphene-supported TiO<sub>2</sub>: Study of promotion of charge carrier in photocatalytic water splitting and methylene blue dye degradation. *Adv. Compos. Hybrid. Mater* **2020**, *3*, 127–140. [[CrossRef](#)]
7. You, B.; Sun, Y. Innovative Strategies for Electrocatalytic Water Splitting. *Acc. Chem. Res.* **2018**, *51*, 1571–1580. [[CrossRef](#)]
8. Zhang, Y.; Huang, Y.; Zhu, S.S.; Liu, Y.Y.; Zhang, X.; Wang, J.J.; Braun, A. Covalent SO Bonding Enables Enhanced Photoelectrochemical Performance of Cu<sub>2</sub>S/Fe<sub>2</sub>O<sub>3</sub> Heterojunction for Water Splitting. *Small* **2021**, *17*, 2100320. [[CrossRef](#)]
9. Liang, J.; Shen, H.; Kong, J. Steel Mesh Reinforced Ni(OH)<sub>2</sub> Nanosheets with Enhanced Oxygen Evolution Reaction Performance. *ES Mater. Manuf.* **2021**, *14*, 79–86. [[CrossRef](#)]
10. Lei, Y.Q.; Xu, T.T.; Ye, S.H.; Zheng, L.R.; Liao, P.; Xiong, W.; Hu, J.; Wang, Y.J.; Wang, J.P.; Ren, X.Z.; et al. Engineering defect-rich Fe-doped NiO coupled Ni cluster nanotube arrays with excellent oxygen evolution activity. *Appl. Catal. B-Environ.* **2021**, *285*, 119809. [[CrossRef](#)]
11. Sun, H.; Yan, Z.; Liu, F.; Xu, W.; Cheng, F.; Chen, J. Self-Supported Transition-Metal-Based Electrocatalysts for Hydrogen and Oxygen Evolution. *Adv. Mater.* **2020**, *32*, 1806326. [[CrossRef](#)] [[PubMed](#)]
12. Pascuzzi, M.E.C.; Hofmann, J.P.; Hensen, E.J.M. Promoting oxygen evolution of IrO<sub>2</sub> in acid electrolyte by Mn. *Electrochim. Acta* **2021**, *366*, 137448. [[CrossRef](#)]
13. Li, S.; Gao, Y.; Li, N.; Ge, L.; Bu, X.; Feng, P. Transition metal-based bimetallic MOFs and MOF-derived catalysts for electrochemical oxygen evolution reaction. *Energy Environ. Sci.* **2021**, *14*, 1897–1927. [[CrossRef](#)]
14. Cai, Z.; Wang, P.; Yang, J.; Wang, X. Update on Recent Designing Strategies of Transition Metal-Based Layered Double Hydroxides Bifunctional electrocatalysts. *ES Energy Environ.* **2019**, *5*, 22–36. [[CrossRef](#)]
15. Ma, Y.; Xie, X.; Yang, W.; Yu, Z.; Sun, X.; Zhang, Y.; Yang, X.; Kimura, H.; Hou, C.; Guo, Z.; et al. Recent advances in transition metal oxides with different dimensions as electrodes for high-performance supercapacitors. *Adv. Compos. Hybrid. Mater* **2021**, *4*, 906–924. [[CrossRef](#)]
16. Guo, Y.; Park, T.; Yi, J.W.; Henzie, J.; Kim, J.; Wang, Z.; Jiang, B.; Bando, Y.; Sugahara, Y.; Tang, J.; et al. Nanoarchitectonics for Transition-Metal-Sulfide-Based Electrocatalysts for Water Splitting. *Adv. Mater.* **2019**, *31*, 1807134. [[CrossRef](#)]
17. Li, Z.; Cai, L.; Song, M.; Shen, Y.; Wang, X.; Li, J.; Wang, J.; Wang, P.; Tian, L. Ternary FeCoNi alloy nanoparticles embedded in N-doped carbon nanotubes for efficient oxygen evolution reaction electrocatalysis. *Electrochim. Acta* **2020**, *339*, 135886. [[CrossRef](#)]
18. Wu, Z.P.; Lu, X.F.; Zang, S.Q.; Lou, X.W. Non-Noble-Metal-Based Electrocatalysts toward the Oxygen Evolution Reaction. *Adv. Funct. Mater.* **2020**, *30*, 1910274. [[CrossRef](#)]
19. Hou, C.; Yang, W.; Xie, X.; Sun, X.; Wang, J.; Naik, N.; Pan, D.; Mai, X.; Guo, Z.; Dang, F.; et al. Agaric-like anodes of porous carbon decorated with MoO<sub>2</sub> nanoparticles for stable ultralong cycling lifespan and high-rate lithium/sodium storage. *J. Colloid. Interface Sci.* **2021**, *596*, 396–407. [[CrossRef](#)]
20. Wu, N.; Du, W.; Hu, Q.; Vupputuri, S.; Jiang, Q. Recent Development in Fabrication of Co Nanostructures and Their Carbon Nanocomposites for Electromagnetic Wave Absorption. *Eng. Sci.* **2020**, *13*, 11–23. [[CrossRef](#)]
21. Feng, L.; Lu, W.; Liu, J.; Li, D.; Hu, L.; Xu, C. Guarding active sites and electron transfer engineering of core-shell nanosheet as robust bifunctional applications for overall water splitting and capacitors. *Electrochim. Acta* **2020**, *331*, 135372. [[CrossRef](#)]
22. Zhao, Q.; Yan, Z.; Chen, C.; Chen, J. Spinels: Controlled Preparation, Oxygen Reduction/Evolution Reaction Application, and Beyond. *Chem. Rev.* **2017**, *117*, 10121–10211. [[CrossRef](#)] [[PubMed](#)]
23. Kim, J.S.; Kim, B.; Kim, H.; Kang, K. Recent Progress on Multimetal Oxide Catalysts for the Oxygen Evolution Reaction. *Adv. Energy Mater.* **2018**, *8*, 1702774. [[CrossRef](#)]
24. Hou, C.; Wang, B.; Murugadoss, V.; Vupputuri, S.; Chao, Y.; Guo, Z.; Wang, C.; Du, W. Recent Advances in Co<sub>3</sub>O<sub>4</sub> as Anode Materials for High-Performance Lithium-Ion Batteries. *Eng. Sci.* **2020**, *11*, 19–30. [[CrossRef](#)]
25. Yang, H.; Liu, Y.; Luo, S.; Zhao, Z.; Wang, X.; Luo, Y.; Wang, Z.; Jin, J.; Ma, J. Lateral-Size-Mediated Efficient Oxygen Evolution Reaction: Insights into the Atomically Thin Quantum Dot Structure of NiFe<sub>2</sub>O<sub>4</sub>. *ACS Catal.* **2017**, *7*, 5557–5567. [[CrossRef](#)]
26. Yuan, F.; Cheng, X.; Wang, M.; Ni, Y. Controlled synthesis of tubular ferrite MFe<sub>2</sub>O<sub>4</sub> (M = Fe, Co, Ni) microstructures with efficiently electrocatalytic activity for water splitting. *Electrochim. Acta* **2019**, *324*, 134883. [[CrossRef](#)]
27. Choi, J.; Kim, D.; Zheng, W.; Yan, B.; Li, Y.; Lee, L.Y.S.; Piao, Y. Interface engineered NiFe<sub>2</sub>O<sub>4</sub>-x/NiMoO<sub>4</sub> nanowire arrays for electrochemical oxygen evolution. *Appl. Catal. B* **2021**, *286*, 119857. [[CrossRef](#)]
28. Liu, J.L.; Zhu, D.D.; Ling, T.; Vasileff, A.; Qiao, S.Z. S-NiFe<sub>2</sub>O<sub>4</sub> ultra-small nanoparticle built nanosheets for efficient water splitting in alkaline and neutral pH. *Nano Energy* **2017**, *40*, 264–273. [[CrossRef](#)]
29. Wu, Z.; Zou, Z.; Huang, J.; Gao, F. NiFe<sub>2</sub>O<sub>4</sub> Nanoparticles/NiFe Layered Double-Hydroxide Nanosheet Heterostructure Array for Efficient Overall Water Splitting at Large Current Densities. *ACS Appl. Mater. Interfaces* **2018**, *10*, 26283–26292. [[CrossRef](#)]
30. Fan, A.; Qin, C.; Zhang, X.; Dai, X.; Dong, Z.; Luan, C.; Yu, L.; Ge, J.; Gao, F. Phosphorus-Doped FeNi Alloys/NiFe<sub>2</sub>O<sub>4</sub> Imbedded in Carbon Network Hollow Bipyramid as Efficient Electrocatalysts for Oxygen Evolution Reaction. *ACS Sustain. Chem. Eng.* **2018**, *7*, 2285–2295. [[CrossRef](#)]
31. Chen, S.; Mao, M.; Liu, X.; Hong, S.; Lu, Z.; Sang, S.; Liu, K.; Liu, H. A High-Rate Cathode Material Hybridized by in-Site Grown Ni-Fe Layered Double Hydroxides and Carbon Black Nanoparticles. *J. Mater. Chem. A* **2016**, *4*, 4877–4881. [[CrossRef](#)]

32. Ali, G.; Park, Y.J.; Hussain, A.; Cho, S.O. A Novel Route to the Formation of 3D Nanoflower-like Hierarchical Iron Oxide Nanostructure. *Nanotechnology* **2019**, *30*, 095601. [[CrossRef](#)] [[PubMed](#)]
33. Kan, S.; Xu, M.; Feng, W.; Wu, Y.; Du, C.; Gao, X.; Wu, Y.A.; Liu, H. Tuning Overall Water Splitting on an Electrodeposited NiCoFeP Films. *ChemElectroChem* **2021**, *8*, 539–546. [[CrossRef](#)]
34. Li, Z.; Deng, S.; Yu, H.; Yin, Z.; Qi, S.; Yang, L.; Lv, J.; Sun, Z.; Zhang, M. Fe–Co–Ni Trimetallic Organic Framework Chrysanthemum-like Nanoflowers: Efficient and Durable Oxygen Evolution Electrocatalysts. *J. Mater. Chem. A* **2022**, *10*, 4230–4241. [[CrossRef](#)]
35. Huang, Y.; Wang, J.-J.; Zou, Y.; Jiang, L.-W.; Liu, X.-L.; Jiang, W.-J.; Liu, H.; Hu, J.-S. Selective Se doping of NiFe<sub>2</sub>O<sub>4</sub> on an active NiOOH scaffold for efficient and robust water oxidation. *Chem. Eng. J.* **2021**, *42*, 1395–1403. [[CrossRef](#)]
36. Chourpa, I.; Douziech-Eyrolles, L.; Ngaboni-Okassa, L.; Fouquenot, J.F.; Cohen-Jonathan, S.; Souce, M.; Marchais, H.; Dubois, P. Molecular composition of iron oxide nanoparticles, precursors for magnetic drug targeting, as characterized by confocal Raman microspectroscopy. *Analyst* **2005**, *130*, 1395–1403. [[CrossRef](#)]
37. Xiao, Y.L.; Zai, J.T.; Li, X.M.; Gong, Y.; Li, B.; Han, Q.Y.; Qian, X.F. Polydopamine functionalized graphene/NiFe<sub>2</sub>O<sub>4</sub> nanocomposite with improving Li storage performances. *Nano Energy* **2014**, *6*, 51–58. [[CrossRef](#)]
38. Landon, J.; Demeter, E.; Inoglu, N.; Keturakis, C.; Wachs, I.E.; Vasic, R.; Frenkel, A.I.; Kitchin, J.R. Spectroscopic Characterization of Mixed Fe–Ni Oxide Electrocatalysts for the Oxygen Evolution Reaction in Alkaline Electrolytes. *ACS Catal.* **2012**, *2*, 1793–1801. [[CrossRef](#)]
39. Zhou, L.J.; Huang, X.; Chen, H.; Jin, P.; Li, G.D.; Zou, X. A high surface area flower-like Ni–Fe layered double hydroxide for electrocatalytic water oxidation reaction. *Dalton Trans.* **2015**, *44*, 11592–11600. [[CrossRef](#)]
40. Hunter, B.M.; Hieringer, W.; Winkler, J.R.; Gray, H.B.; Müller, A.M. Effect of interlayer anions on [NiFe]-LDH nanosheet water oxidation activity. *Energy Environ. Sci.* **2016**, *9*, 1734–1743. [[CrossRef](#)]
41. Chen, X.; Zeng, Y.; Chen, Z.; Wang, S.; Xin, C.; Wang, L.; Shi, C.; Lu, L.; Zhang, C. Synthesis and Electrochemical Property of FeOOH/Graphene Oxide Composites. *Front. Chem.* **2020**, *8*, 328. [[CrossRef](#)] [[PubMed](#)]
42. Safi, S.R.; Senmoto, K.; Gotoh, T.; Iizawa, T.; Nakai, S. The effect of gamma-FeOOH on enhancing arsenic adsorption from groundwater with DMAPAAQ + FeOOH gel composite. *Sci. Rep.* **2019**, *9*, 11909. [[CrossRef](#)] [[PubMed](#)]
43. Xu, N.; Zhang, Y.; Zhang, T.; Liu, Y.; Qiao, J. Efficient quantum dots anchored nanocomposite for highly active ORR/OER electrocatalyst of advanced metal–air batteries. *Nano Energy* **2019**, *57*, 176–185. [[CrossRef](#)]
44. Liu, X.; Guo, R.; Ni, K.; Xia, F.; Niu, C.; Wen, B.; Meng, J.; Wu, P.; Wu, J.; Wu, X.; et al. Reconstruction-Determined Alkaline Water Electrolysis at Industrial Temperatures. *Adv. Mater.* **2020**, *32*, 2001136. [[CrossRef](#)]
45. Kuai, C.; Xi, C.; Hu, A.; Zhang, Y.; Xu, Z.; Nordlund, D.; Sun, C.-J.; Cadigan, C.A.; Richards, R.M.; Li, L.; et al. Revealing the Dynamics and Roles of Iron Incorporation in Nickel Hydroxide Water Oxidation Catalysts. *J. Am. Chem. Soc.* **2021**, *143*, 18519–18526. [[CrossRef](#)] [[PubMed](#)]
46. Stevens, M.B.; Enman, L.J.; Batchellor, A.S.; Cosby, M.R.; Vise, A.E.; Trang, C.D.M.; Boettcher, S.W. Measurement Techniques for the Study of Thin Film Heterogeneous Water Oxidation Electrocatalysts. *Chem. Mat.* **2017**, *29*, 120–140. [[CrossRef](#)]
47. Wang, J.; Gao, Y.; Kong, H.; Kim, J.; Choi, S.; Ciucci, F.; Hao, Y.; Yang, S.; Shao, Z.; Lim, J. Non-precious-metal catalysts for alkaline water electrolysis: Operando characterizations, theoretical calculations, and recent advances. *Chem. Soc. Rev.* **2020**, *49*, 9154–9196. [[CrossRef](#)]
48. Sun, H.; Qin, D.; Huang, S.; Guo, X.; Li, D.; Luo, Y.; Meng, Q. Dye-sensitized solar cells with NiS counter electrodes electrodeposited by a potential reversal technique. *Energy Environ. Sci.* **2011**, *4*, 2630–2637. [[CrossRef](#)]
49. Xu, Q.; Jiang, H.; Duan, X.; Jiang, Z.; Hu, Y.; Boettcher, S.W.; Zhang, W.; Guo, S.; Li, C. Fluorination-enabled Reconstruction of NiFe Electrocatalysts for Efficient Water Oxidation. *Nano Lett.* **2021**, *21*, 492–499. [[CrossRef](#)]
50. Zhou, Y.; Wang, Z.; Pan, Z.; Liu, L.; Xi, J.; Luo, X.; Shen, Y. Exceptional Performance of Hierarchical Ni–Fe (hydr)oxide@NiCu Electrocatalysts for Water Splitting. *Adv. Mater.* **2019**, *31*, 1806769. [[CrossRef](#)]
51. Anantharaj, S.; Ede, S.R.; Karthick, K.; Sankar, S.S.; Sangeetha, K.; Karthik, P.E.; Kundu, S. Precision and correctness in the evaluation of electrocatalytic water splitting: Revisiting activity parameters with a critical assessment. *Energy Environ. Sci.* **2018**, *11*, 744–771. [[CrossRef](#)]
52. Gu, Y.; Pan, Z.; Zhang, H.; Zhu, J.; Yuan, B.; Pan, D.; Wu, C.; Dong, B.; Guo, Z. Synthesis of high performance diesel oxidation catalyst using novel mesoporous AlLaZrTiOx mixed oxides by a modified sol-gel method. *Adv. Compos Hybrid. Mater.* **2020**, *3*, 583–593. [[CrossRef](#)]
53. Khan, S.H.; Pathak, B.; Fulekar, M.H. A study on the influence of metal (Fe, Bi, and Ag) doping on structural, optical, and antimicrobial activity of ZnO nanostructures. *Adv. Compos Hybrid. Mater.* **2020**, *3*, 551–569. [[CrossRef](#)]
54. Cui, M.; Yang, C.; Li, B.; Dong, Q.; Wu, M.; Hwang, S.; Xie, H.; Wang, X.; Wang, G.; Hu, L. High-Entropy Metal Sulfide Nanoparticles Promise High-Performance Oxygen Evolution Reaction. *Adv. Energy Mater.* **2020**, *11*, 2002887. [[CrossRef](#)]
55. Zhang, H.; Li, X.; Hähnel, A.; Naumann, V.; Lin, C.; Azimi, S.; Schweizer, S.L.; Maijenburg, A.W.; Wehrspohn, R.B. Bifunctional Heterostructure Assembly of NiFe LDH Nanosheets on NiCoP Nanowires for Highly Efficient and Stable Overall Water Splitting. *Adv. Funct. Mater.* **2018**, *28*, 1706847. [[CrossRef](#)]
56. Wang, B.; Zhao, K.; Yu, Z.; Sun, C.; Wang, Z.; Feng, N.; Mai, L.; Wang, Y.; Xia, Y. In situ structural evolution of the multi-site alloy electrocatalyst to manipulate the intermediate for enhanced water oxidation reaction. *Energy Environ. Sci.* **2020**, *13*, 2200–2208. [[CrossRef](#)]

57. Li, X.-L.; Yang, G.-Q.; Li, S.-S.; Xiao, N.; Li, N.; Gao, Y.-Q.; Lv, D.; Ge, L. Novel dual co-catalysts decorated Au@HCS@PdS hybrids with spatially separated charge carriers and enhanced photocatalytic hydrogen evolution activity. *Chem. Eng. J.* **2020**, *379*, 122350. [[CrossRef](#)]
58. Mabayoje, O.; Shoola, A.; Wygant, B.R.; Mullins, C.B. The Role of Anions in Metal Chalcogenide Oxygen Evolution Catalysis: Electrodeposited Thin Films of Nickel Sulfide as “Pre-catalysts”. *ACS Energy Lett.* **2016**, *1*, 195–201. [[CrossRef](#)]
59. He, F.; Huang, Z.; Wei, G.; Zhao, K.; Wang, G.; Kong, X.; Feng, Y.; Tan, H.; Hou, S.; Lv, Y.; et al. Biomass chemical-looping gasification coupled with water/CO<sub>2</sub>-splitting using NiFe<sub>2</sub>O<sub>4</sub> as an oxygen carrier. *Energy Convers. Manag.* **2019**, *201*, 112157.
60. Domínguez-Arvizu, J.L.; Jiménez-Miramontes, J.A.; Salinas-Gutiérrez, J.M.; Meléndez-Zaragoza, M.J.; López-Ortiz, A.; Collins-Martínez, V. Study of NiFe<sub>2</sub>O<sub>4</sub> nanoparticles optical properties by a six-flux radiation model towards the photocatalytic hydrogen production. *Int. J. Hydrogen Energy* **2019**, *44*, 12455–12462. [[CrossRef](#)]
61. Shinde, P.V.; Mane, P.; Chakraborty, B.; Sekhar Rout, C. Spinel NiFe<sub>2</sub>O<sub>4</sub> nanoparticles decorated 2D Ti<sub>3</sub>C<sub>2</sub> MXene sheets for efficient water splitting: Experiments and theories. *J. Colloid. Interface. Sci.* **2021**, *602*, 232–241. [[CrossRef](#)] [[PubMed](#)]
62. Zhao, X.J.; Pachfule, P.; Li, S.; Simke, J.R.J.; Schmidt, J.; Thomas, A. Bifunctional Electrocatalysts for Overall Water Splitting from an Iron/Nickel-Based Bimetallic Metal-Organic Framework/Dicyandiamide Composite. *Angew. Chem.-Int. Edit.* **2018**, *57*, 8921–8926. [[CrossRef](#)] [[PubMed](#)]
63. Zhong, H.; Gao, G.; Wang, X.; Wu, H.; Shen, S.; Zuo, W.; Cai, G.; Wei, G.; Shi, Y.; Fu, D.; et al. Ion Irradiation Inducing Oxygen Vacancy-Rich NiO/NiFe<sub>2</sub>O<sub>4</sub> Heterostructure for Enhanced Electrocatalytic Water Splitting. *Small* **2021**, *17*, e2103501. [[CrossRef](#)] [[PubMed](#)]
64. Karpuraranjith, M.; Chen, Y.; Wang, B.; Ramkumar, J.; Yang, D.; Srinivas, K.; Wang, W.; Zhang, W.; Manigandan, R. Hierarchical ultrathin layered MoS<sub>2</sub>@NiFe<sub>2</sub>O<sub>4</sub> nanohybrids as a bifunctional catalyst for highly efficient oxygen evolution and organic pollutant degradation. *J. Colloid. Interface. Sci.* **2021**, *592*, 385–396. [[CrossRef](#)] [[PubMed](#)]
65. Liang, X.; Weng, W.; Gu, D.; Xiao, W. Nickel based oxide film formed in molten salts for efficient electrocatalytic oxygen evolution. *J. Mater. Chem. A* **2019**, *7*, 10514–10522. [[CrossRef](#)]